

Exploring, tailoring, and traversing the solution landscape of a phase-shaped CARS process

Alexander C.W. van Rhijn, Herman L. Offerhaus, Peter van der Walle,
Jennifer L. Herek, and Aliakbar Jafarpour*

Optical Sciences group, MESA⁺ Institute for Nanotechnology, University of Twente, Enschede, The Netherlands
*jafarpoura@gmail.com

Abstract: Pulse shaping techniques are used to improve the selectivity of broadband CARS experiments, and to reject the overwhelming background. Knowledge about the fitness landscape and the capability of tailoring it is crucial for both fundamental insight and performing an efficient optimization of phase shapes. We use an evolutionary algorithm to find the optimal spectral phase of the broadband pump and probe beams in a background-suppressed shaped CARS process. We then investigate the shapes, symmetries, and topologies of the landscape contour lines around the optimal solution and also around the point corresponding to zero phase. We demonstrate the significance of the employed phase bases in achieving convex contour lines, suppressed local optima, and high optimization fitness with a few (and even a single) optimization parameter.

©2010 Optical Society of America

OCIS codes: (300.6230) Spectroscopy, coherent anti-Stokes Raman scattering; (320.5540) Pulse shaping; (170.5660) Raman spectroscopy; (180.5655) Raman microscopy; (320.0320) Ultrafast optics; (260.7120) Ultrafast phenomena.

References and links

1. J.-X. Cheng, and X. S. Xie, "Coherent Anti-Stokes Raman Scattering Microscopy: Instrumentation, Theory, and Applications," *J. Phys. Chem. B* **108**(3), 827–840 (2004).
2. M. Juma, J. P. Kortarik, C. Otto, J. L. Herek, and H. L. Offerhaus, "Vibrational phase contrast microscopy by use of coherent anti-Stokes Raman scattering," *Phys. Rev. Lett.* **103**(4), 043905 (2009).
3. D. Oron, N. Dudovich, D. Yelin, and Y. Silberberg, "Quantum control of coherent anti-Stokes Raman processes," *Phys. Rev. A* **65**(4), 043408 (2002).
4. P. Brumer, and M. Shapiro, "Control of unimolecular reactions using coherent light," *Chem. Phys. Lett.* **126**(6), 541–546 (1986).
5. R. S. Judson, and H. Rabitz, "Teaching lasers to control molecules," *Phys. Rev. Lett.* **68**(10), 1500–1503 (1992).
6. J. L. Herek, W. Wohlleben, R. J. Cogdell, D. Zeidler, and M. Motzkus, "Quantum control of energy flow in light harvesting," *Nature* **417**(6888), 533–535 (2002).
7. D. Meshulach, and Y. Silberberg, "Coherent quantum control of multiphoton transitions by shaped ultrashort optical pulses," *Phys. Rev. A* **60**(2), 1287–1292 (1999).
8. J. X. Chen, A. Volkmer, L. D. Book, *et al.*, "Multiplex coherent anti-stokes Raman scattering microspectroscopy and study of lipid vesicles," *J. Phys. Chem. B* **106**(34), 8493–8498 (2002).
9. N. Dudovich, D. Oron, and Y. Silberberg, "Single-pulse coherently controlled nonlinear Raman spectroscopy and microscopy," *Nature* **418**(6897), 512–514 (2002).
10. S.-H. Lim, A. G. Caster, O. Nicolet, and S. R. Leone, "Chemical imaging by single pulse interferometric coherent anti-stokes Raman scattering microscopy," *J. Phys. Chem. B* **110**(11), 5196–5204 (2006).
11. B.-C. Chen, and S.-H. Lim, "Optimal laser pulse shaping for interferometric multiplex coherent anti-stokes Raman scattering microscopy," *J. Phys. Chem. B* **112**(12), 3653–3661 (2008).
12. B. vonvacano, and M. Motzkus, "Time-resolved two color single-beam CARS employing supercontinuum and femtosecond pulse shaping," *Opt. Commun.* **264**(2), 488–493 (2006).
13. D. Pestov, R. K. Murawski, G. O. Ariunbold, X. Wang, M. Zhi, A. V. Sokolov, V. A. Sautenkov, Y. V. Rostovtsev, A. Dogariu, Y. Huang, and M. O. Scully, "Optimizing the laser-pulse configuration for coherent Raman spectroscopy," *Science* **316**(5822), 265–268 (2007).
14. S. O. Konorov, X. G. Xu, R. F. Turner, M. W. Blades, J. W. Hepburn, and V. Milner, "Pulse optimization for Raman spectroscopy with cross-correlation frequency resolved optical gating," *Opt. Express* **15**(12), 7564–7571 (2007).
15. J. Konradi, A. K. Singh, A. V. Scaria, and A. Materny, "Selective spectral filtering of molecular modes of beta-carotene in solution using optimal control in four-wave-mixing spectroscopy," *J. Raman Spectrosc.* **37**(6), 697–704 (2006).

16. S. Pezeshki, M. Schreiber, and U. Kleinekathöfer, "Shaping femtosecond coherent anti-Stokes Raman spectra using optimal control theory," *Phys. Chem. Chem. Phys.* **10**(15), 2058–2066 (2008).
17. S. Zhang, L. Zhang, X. Zhang, L. Ding, G. Chen, Z. Sun, and Z. Wang, "Selective excitation of CARS by adaptive pulse shaping based on genetic algorithm," *Chem. Phys. Lett.* **433**(4–6), 416–421 (2007).
18. J. Konradi, A. K. Singh, and A. Materny, "Mode-focusing in molecules by feedback-controlled shaping of femtosecond laser pulses," *Phys. Chem. Chem. Phys.* **7**, 3574–3579 (2005).
19. A. M. Weiner, D. E. Leaird, P. G. Wiederrecht, and K. A. Nelson, "Femtosecond multiple-pulse impulsive stimulated Raman scattering spectroscopy," *J. Opt. Soc. Am. B* **8**(6), 1264–1275 (1991).
20. H. Li, D. A. Harris, B. Xu, P. J. Wrzesinski, V. V. Lozovoy, and M. Dantus, "Coherent mode-selective Raman excitation towards standoff detection," *Opt. Express* **16**(8), 5499–5504 (2008).
21. X. G. Xu, S. O. Konorov, J. W. Hepburn, and V. Milner, "Noise autocorrelation spectroscopy with coherent Raman scattering," *Nat. Phys.* **4**(2), 125–129 (2008).
22. S. Mukamel, "Controlling multidimensional off-resonant-Raman and infrared vibrational spectroscopy by finite pulse band shapes," *J. Chem. Phys.* **130**(5), 054110 (2009).
23. J. J. Song, G. L. Eesley, and M. D. Levenson, "Background suppression in coherent Raman spectroscopy," *Appl. Phys. Lett.* **29**(9), 567 (1976).
24. Y. J. Lee, and M. T. Cicerone, "Single-shot interferometric approach to background free broadband coherent anti-Stokes Raman scattering spectroscopy," *Opt. Express* **17**(1), 123–135 (2009).
25. S.-H. Lim, A. G. Caster, and S. R. Leone, "Fourier transform spectral interferometric coherent anti-Stokes Raman scattering (FTSI-CARS) spectroscopy," *Opt. Lett.* **32**(10), 1332–1334 (2007).
26. Y. Liu, Y. J. Lee, and M. T. Cicerone, "Fast extraction of resonant vibrational response from CARS spectra with arbitrary nonresonant background," *J. Raman Spectrosc.* **40**(7), 726–731 (2009).
27. S. Postma, A. C. W. van Rhijn, J. P. Korterik, P. Gross, J. L. Herek, and H. L. Offerhaus, "Application of spectral phase shaping to high resolution CARS spectroscopy," *Opt. Express* **16**(11), 7985–7996 (2008).
28. A. C. W. van Rhijn, S. Postma, J. P. Korterik, J. L. Herek, and H. L. Offerhaus, "Chemically selective imaging by spectral phase shaping for broadband CARS around 3000 cm^{-1} ," *J. Opt. Soc. Am. B* **26**(3), 559–563 (2009).
29. P. van der Walle, H. L. Offerhaus, J. L. Herek, and A. Jafarpour, "Tailoring a coherent control solution landscape by linear transforms of spectral phase basis," *Opt. Express* **18**(2), 973–987 (2010).
30. L. Cheng, and D. Y. Kim, "Differential imaging in coherent anti-Stokes Raman scattering microscopy with Laguerre-Gaussian excitation beams," *Opt. Express* **15**(16), 10123–10134 (2007).
31. S. A. Malinovskaya, and V. S. Malinovsky, "Chirped-pulse adiabatic control in coherent anti-Stokes Raman scattering for imaging of biological structure and dynamics," *Opt. Lett.* **32**(6), 707–709 (2007).
32. Y. Silberberg, "Quantum coherent control for nonlinear spectroscopy and microscopy," *Annu. Rev. Phys. Chem.* **60**(1), 277–292 (2009).
33. T. Brixner, N. H. Damrauer, B. Kiefer, and G. Gerber, "Liquid-phase adaptive femtosecond quantum control: Removing intrinsic intensity dependencies," *J. Chem. Phys.* **118**(8), 3692 (2003).
34. N. Hansen, "The CMA evolution strategy: a tutorial," <http://www.lri.fr/~hansen/cmatutorial.pdf>.
35. R. Fanciulli, L. Willmes, J. Savolainen, P. van der Walle, T. Bäck, and J. L. Herek, "Evolution strategies for laser pulse compression," *Lect. Notes Comput. Sci.* **4926**, 219–230 (2008).
36. P. S. C. Heuberger, P. M. J. Van den Hof, and B. Wahlberg, *Modelling and Identification with Rational Orthogonal Basis Functions* (Springer, 2005).
37. M. Telescu, N. Tanguy, P. Bréhonnet, and P. Vilbé, "Efficient Gram-matrix computation for irrational resonant systems using Kautz models," *Signal Process.* **87**(12), 3234–3240 (2007).
38. A. Jafarpour, J. Savolainen, R. de Jong, J. Middag, D. P. Sprünken, P. van der Walle, D. Yang, and J. L. Herek, "Robust orthogonal parameterization of evolution strategy for adaptive laser pulse shaping," *Opt. Express* **17**(14), 11986–12000 (2009).
39. N. Hansen, "Tutorial: Covariance Matrix Adaptation (CMA) Evolution Strategy," Institute of Computational Science, ETH Zurich, September 2006 PPSN 2006.
40. R. E. Kalman, "Canonical structure of linear dynamical systems," *Proc. Natl. Acad. Sci. U.S.A.* **48**(4), 596–600 (1962).
41. U. Forssell, and L. Ljung, "Closed-loop identification revisited," *Automatica* **35**(7), 1215–1241 (1999).
42. B. Nouri, R. Achar, M. Nakhla, and D. Saraswat, "z-Domain Orthonormal Vector Fitting for Macromodeling High-Speed Modules Characterized by Tabulated Data," in *Proc. 12th IEEE Workshop on Signal Propagation on Interconnects (SPI 2008)*, pp. 1–4, DOI: 10.1109/SPI.2008.4558378.

1. Introduction

Coherent anti-Stokes Raman scattering (CARS) is the basis of a powerful microspectroscopic technique for probing Raman-active vibrational levels of materials. Compared to the conventional incoherent Raman spectroscopy, CARS has the advantages of generating stronger signals, a spectrum separated from that of fluorescence, and easier collimation due to a more directional radiation pattern. Microscopy with CARS yields not only chemical selectivity, but also an inherent spatial resolution typical of nonlinear microscopic techniques. Picosecond laser pulses are commonly used in CARS experiments to achieve sufficiently

high peak intensities with just a few mW of average power per beam, and sufficiently narrow bandwidths to achieve a reasonable spectral resolution of a few cm^{-1} [1,2].

One major drawback of CARS experiments using narrowband picosecond lasers is the need for tunable laser source(s). It prevents real-time measurements over a spectral range. An alternative CARS scheme employs broadband femtosecond laser pulses to probe a range of vibrational levels without changing the pump center wavelength. The low spectral resolution or poor chemical selectivity of such a CARS experiment can be overcome by pulse shaping, as in coherent control experiments [3]. Coherent control tailors the photo-induced energy flow in a sample by appropriate laser pulse shaping [4–6], and provides characteristic signatures for two- and multi-photon transitions [7].

CARS experiments with shaped laser pulses span a wide range of configurations. While the pioneer studies used non-degenerate (three different) sources as the pump, the probe, and the Stokes beams [3], later experiments have used two [8] or even just one single pulse [9–11]. The detection schemes include not only the measurement of the total CARS signal energy, but also resolving the CARS signal in the frequency and time-frequency domains [12–15]. The optimization of the CARS selectivity has been reported using both (semi-) analytical [16] and numerical techniques [17,18]. Similar to the models used in telecommunications, binary profiles [19,20] (in addition to conventional continuous profiles) have been employed for pulse shaping. Two recent types of coherent Raman spectroscopy with tailored pulses are based on uncorrelated (“noisy”) phase profiles [21] and multi-dimensional excitations [22].

An ideal CARS measurement only probes the (vibrationally) resonant Raman signal. In practice, both the resonant Raman and a non-resonant background signal contribute to the CARS signal (Fig. 1). The sensitivity of a CARS measurement is generally limited not by the signal to noise ratio, rather by distinguishing the resonant CARS signal embedded in a strong non-resonant background signal. An older technique for background-free CARS measurement is based on a specific polarization configuration of the pump, the probe, and the Stokes beams [23]. Since the background signal has a real and nearly flat $\chi^{(3)}$ profile, CARS experiments with shaped pulses can suppress the background signal, and achieve nearly background-free signals. These techniques can be put into three main categories: a) temporally offsetting a narrowband probe pulse [13,24], b) using the causality of the CARS signal and employing the nonresonant background as a local oscillator in Fourier transform spectral interferometry (FTSI) [25,26], and c) using the time-reversal asymmetry in experiments with a degenerate broadband pump (= probe) [27,28].

A key question regarding shaped CARS experiments in general, and those performing an optimization in particular, is the shape and the topology of the solution space with each point representing a phase function and the associated fitness. Ideally, the contour lines are convex, connected (no local optima), and without nonlinear shear (relative rotation) [29]. It will also be very useful to have separable phase terms to find the projections of the optimal phase on each phase coordinate (the weights of different basis functions) separately via 1D scans. Identifying the shape and the topology of the contour lines and tailoring them towards aforementioned ideal shapes and topologies is the aim of this contribution.

We first discuss the profile of the optimal phase of a background-suppressed CARS experiment qualitatively. We then use an evolutionary optimization algorithm to determine the optimal phase quantitatively. To get more insight into the problem, we fully investigate the 1D, 2D, and 3D solution spaces of a background-suppressed shaped CARS process by employing different basis sets for spectral phase parameterization. These landscapes are calculated both close to the optimal phase and close to the zero phase. Note that our study is focused on a CARS process with a specific choice of narrowband and broadband pulses (as the pump, the Stokes, and the probe beams) [27,28], a specific fitness function, and specific materials. While the quantitative results may not be directly applicable to other shaped CARS experiments, the methodology and the concepts are insightful in those cases, as well.

2. Basic concepts

2.1. CARS process

The spatiotemporal evolution of electromagnetic waves in a CARS process is shown in Fig. 1. The incident electric field experiences Fresnel-like changes in the amplitude and phase upon passing the input facet of the sample. Within the sample, the total electric field E , the total magnetic field H , and the polarization vector, form a coupled-variable process. After another Fresnel-like distortion at the end facet, the electric field leaves the sample with a blue-shifted component, E_{CARS} .

In our study, the Fresnel-like changes at the input and output facets of the sample under test are assumed to be negligible, or at most introduce a frequency-independent attenuation factor. Hence, $E_{z=0}^+$ and $E_{z=L}^-$ are proportional to the observable quantities of E_{inc} and E_{out} , respectively. We also approximate the distributed nature of electrodynamics in the sample by an effective response of a localized molecular system. Under these conditions and by further discarding the contribution of the generated CARS signal to the nonlinear polarization, the blue-shifted component of E_{out} (E_{CARS}) can be approximated by a monotonically-increasing (and for small signals, a linear) function of the magnitude of the driving force; i.e., the third order nonlinear polarization P_{NL} . While a distributed model of $\chi^{(3)}$ can reveal details of CARS spatiotemporal evolution [30], the aforementioned approximations are commonly used for a reasonably accurate description of the microscopic dynamics. It is also assumed here that the pump, the probe, and the Stokes beams have peak intensities below the threshold of strong-field effects such as energy level Stark shift [31,32], even at zero delay (full overlap) of transform-limited pulses.

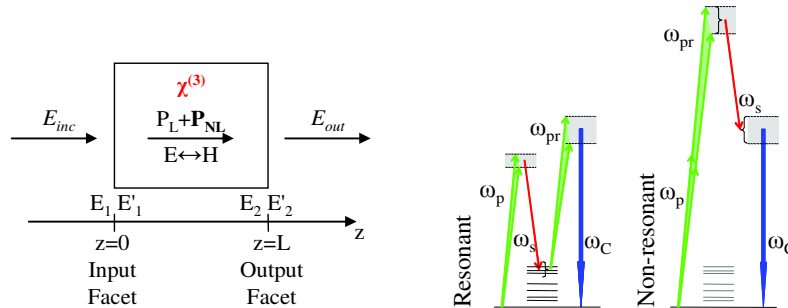


Fig. 1. Semi-classical description of the CARS process: (left) coupled interactions of the electric field E , the magnetic field H , and the linear/nonlinear components of polarization P_L/P_{NL} , and (right) the energy diagrams of resonant and non-resonant CARS, showing the pump (= probe), the Stokes, and the CARS beams in green, red, and blue, respectively.

2.2. Optimal phase profile

The energy level diagram of the CARS process is shown in Fig. 1 (right). In the resonant CARS process, a broadband pump and a narrowband Stokes beam create a vibrational coherence that nonlinearly scatters off a broadband probe beam. This CARS scheme projects the shaped pump profile to the vibrational frequencies directly and without changing it. It also extends the spectral range of shaped CARS experiments with typical laser lines to the $\sim 3000\text{cm}^{-1}$ region of vibrational frequencies in a single-shot geometry [27,28]. Figure 1 (right) shows that the same beams also participate in another unwanted nonlinear process, which gives rise to a non-resonant background signal at the same wavelength as the resonant CARS signal.

Assuming the same broadband profile E for the pump and the probe beams, a narrowband Stokes beam, and a third order molecular response χ , the nonlinear polarization can be written, within a constant factor corresponding to the amplitude of the Stokes signal, as $P_{\text{NL}}(\omega) = \int E(\omega-\Omega)E(\omega_s + \Omega)\chi(\Omega)d\Omega$, where Ω , ω_s , and ω correspond to a vibrational frequency

variable, the constant Stokes frequency, and CARS frequency variable, respectively. If the phase profiles of the pump electric field envelope and the molecular response are denoted by φ and φ_χ respectively, the Cauchy-Schwarz upper bound of the CARS signal corresponds to $\varphi(\omega_s + \Omega) + \varphi(\omega - \Omega) + \varphi_\chi(\Omega) = b_\omega$; i.e., the net phase of the integrand should be a constant function of the *variable* Ω , but possibly with a dependence on the *parameter* ω . By separating the terms with/without ω , we can write $\varphi(\omega_s + \Omega) + \varphi_\chi(\Omega) = C = b_\omega - \varphi(\omega - \Omega)$, where C is a constant. The first equation implies that the phase of the pump field, aside from a Stokes shift, is the negative of the phase of the molecular response function. By rewriting the second equation as $C - b_\omega = -\varphi(\omega - \Omega)$, the independence of the left-hand side from Ω requires the pump phase function to be a constant (or equivalently zero, by assuming a many-cycle pulse and discarding the carrier envelope phase).

The two aforementioned conditions ($\varphi = -\varphi_\chi$ and $\varphi = 0$) cannot be satisfied simultaneously, as the molecular response function does not have a constant phase. As such, the maximum CARS signal will be smaller than the Cauchy-Schwarz upper bound; i.e., $P_{NL}(\omega)$ with a zero-phase integrand. Note that a key question in many nonlinear optical processes using shaped pulses is whether the optimal solution originates from a *trivial* solution of increasing the peak power (by a flat phase profile) or a *nontrivial* solution originating from the sample dynamics [33]. An interesting interpretation of the two aforementioned and inconsistent constraints on the pump phase profile is that maximizing the CARS signal is a multi-objective optimization comprising and compromising both trivial ($\varphi = 0$) and nontrivial ($\varphi = -\varphi_\chi$) mechanisms.

In order to consider the contributions of all possible Raman lines over the spectral span of the pump spectrum, we consider the total energy of the CARS signal $\|P_{NL}(\omega)\|^2$, where $\|\cdot\|$ denotes the Euclidean norm. Also in order to suppress the background signal, we consider the difference between the energies of two shaped CARS processes with opposite applied phase shapes to define the optimization fitness [27,28]. For any phase profile $\varphi(\omega)$, we first find $F(\varphi) = \|P_{+\varphi}(\omega)\|^2 - \|P_{-\varphi}(\omega)\|^2$, where $P(\omega)$ denotes merely the nonlinear component of polarization. The fitness is then defined as $F_{norm} = F(\varphi)/F(\varphi_{mol})$, where φ_{mol} denotes the phase of the molecular response.

The pump phase profile corresponding to the maximum CARS signal $P_{NL}(\omega)$ is not necessarily $\varphi = -\varphi_\chi$. However, a partial satisfaction of this optimization goal is expected from a pump phase following and compensating the (variation) features of φ_χ . Although this conclusion is based on maximizing the CARS signal at a single frequency ω , it considers the nonlinear intra-pulse interferences of all pump frequencies. This conclusion is obtained for each and all of CARS frequencies, and mainly concerns the variations (not the non-resonant baseline) of χ . As such, the pump phase optimizing $F(\varphi) = \|P_{+\varphi}(\omega)\|^2 - \|P_{-\varphi}(\omega)\|^2$ is also expected to have features corresponding to, but out of phase from, those of φ_χ .

If φ_{opt} is the optimal solution, then both $+\varphi_{opt}$ and $-\varphi_{opt}$ will result in the same absolute value of the fitness F_{norm} , but with different signs. Since $F(\varphi_{mol})$ is negative, the optimal profile maximizing $F_{norm} = F(\varphi)/F(\varphi_{mol})$ is expected to have features corresponding to, and in phase with, those of φ_χ .

2.3. Phase shaping for background signal rejection

The difference between the positive and negative phase rejects the solutions that would optimize on the non-resonant rather than the resonant part of the signal. It does however allow for mixing between the non-resonant and the resonant part to optimize the selective signal. Furthermore, it corresponds to a measurement sequence that is easily implemented and does not require post processing or assumptions about the absolute intensity levels or non-resonant component subtraction.

Note that the background signal shown schematically in Fig. 1 (right) originates from unwanted four-wave mixing processes in the sample under study. Another contribution to the background molecular response originates from the Raman response of the solvent. If the Raman lines of the solvent are sufficiently far from or narrower than the Raman lines of the

sample under study, the total background $\chi^{(3)}$ will still have a real and flat profile, and the aforementioned fitness functions suppresses the background component.

2.4. Solution landscape

The solution landscape of an optimization fitness is a space with each point representing a phase function (candidate solution) and the associated fitness. The optimization is equivalent to traversing a trajectory and crossing contour lines in this space, starting from a point on the contour associated with the initial fitness, and ideally ending on the contour (point) associated with the global optimum. Connected and convex contour lines result in smooth optimization trajectories from any point on the contour associated with the initial fitness to the contour associated with the global optimum. Issues like robustness (or sensitivity) of the optimization to noise are also related to the shape of the contour lines. Furthermore, if the contour lines can be expressed by a separable function of phase terms, the global optimum can be found by a series of 1D scans along each phase coordinate, rather than searching all possible permutations of phase terms [29].

Theoretically, a shaped CARS problem can have an infinite-dimensional solution landscape or functional space. We refer to this space as the *global* solution landscape. By modeling the spectral phase with a specific basis set, such as polynomials, a specific subset of the landscape is selected. Unless otherwise specified, the term “solution landscape” refers to such subsets of the global landscape in the rest of this article. These landscapes can have similar or different properties compared to each other and compared to the global landscape.

3. Calculation of the optimal phase

We consider a CARS process in bulk polystyrene, as in our previous study [27]. A constant non-resonant $\chi^{(3)}$ with an amplitude equal to 12% of the main peak of the resonant $\chi^{(3)}$ (at 3052cm^{-1}) is used in our model. The amplitude and phase of polystyrene $\chi^{(3)}$ are shown in Fig. 2. The pump spectrum has been shifted by the Stokes frequency in Fig. 2 to account for the nonlinear multi-photon process and also for easy comparison with the molecular response spectrum. The spectra of the pump and the Stokes electric fields are centered at 12500 and 9396cm^{-1} (800 and 1064nm), respectively. The pump spectrum has a full-width at half maximum (FWHM) bandwidth of 400cm^{-1} (25.6nm), and the Stokes pulse has a negligible bandwidth and is modeled by a Dirac delta function in the frequency domain.

While 4096 samples are used to model the discretized spectral span of the pump pulse with a resolution of 1cm^{-1} , only 1021 points in the middle of the spectral range are used for shaping. The (unknown) pump phase function over this 1021-point region is further decimated to P points. The values of the pump phase function at these P points are calculated by the optimization algorithm, and the 1021 points of the phase function are then estimated by spline interpolation.

We use a class of evolutionary algorithms, known as evolution strategy (ES), to solve the optimization problem by trying an initial spectral phase profile and successive iterations. The employed ES uses the covariance matrix of parameters to continuously rotate and adapt the set of candidate solutions, and is referred to as covariance matrix adaptation evolution strategy (CMA-ES) [34]. Details of the code implementing CMA-ES are reported elsewhere [35].

As in previous studies, the code is used with a population size of 40, 20 parents, and an initial step size of 10%. Many combinations of CMA parameters have been tried, and the program has approached almost the same optimal phase profile and the same fitness value in all these cases. With $P = 20$ parameters, a maximum fitness of $F_{\text{norm}} = 2.011 (\pm 0.05\%)$ is obtained after about 100 generations. Running the optimization from the 50th to the 100th generation increases the final fitness by less than 0.8%. Increasing the number of parameters from 20 to 30 increases the maximum fitness by only 0.42% (to $F_{\text{norm}} = 2.020$). Several runs of the optimization program with other values of P between 20 and 80 and with proportionally increased number of generations have been considered. In all cases, the same

optimal profiles have been obtained after a few generations. The maximum value of the final fitness for these settings of parameters has been 2.048. It implies that the slight increase in the fitness by significant (up to 4-fold) increase of the number of parameters is due to smaller interpolation errors and not finding an optimal phase profile with different features. The optimal phase profile found using the CMA-ES algorithm and the amplitude of the pump electric field are also shown in Fig. 2. Note the similarities between the profiles of the molecular response and the optimal phase profile, as discussed before.

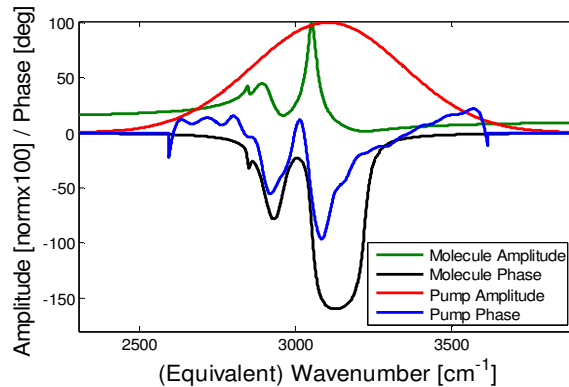


Fig. 2. Amplitude/phase of polystyrene Raman spectrum and Stokes-shifted excitation pulse.

4. Solution landscapes around the optimal point

Once the solution to the optimization problem is known, the landscapes around this point can be calculated by considering the phase function $\varphi = \varphi_{\text{opt}} + \varphi_{\text{excess}}$, where φ_{opt} denotes the optimal phase profile and φ_{excess} is an excess phase profile superimposed on φ_{opt} , the parameters of which are scanned.

While polynomials are successfully used to model the phase shifts associated with the tail of a resonance (as in material dispersion), they are not expected to be that efficient in modeling the sharp features and the flat regions associated with a Lorentzian resonance, simultaneously. Hence, in addition to polynomials, we also consider the alternative basis sets of rational functions [36] in the study of the CARS landscape. A rational function is one that can be written as the ratio of two polynomials, such as a sum of some Lorentzian functions. As a truncated Laurent series, a rational function can be useful in modeling a function without a Taylor series, or one requiring many orders of Taylor series and thereby enhancing numerical errors. We restrict ourselves to a specific type of rational functions in Sections 4 and 5, and will consider them in a more general sense in the Discussion Section.

The rational Kautz basis set used here comprises alternatively even and odd functions in the Laplace (complex frequency) domain, as $\psi_{2n}(s) = [(2bc)^{0.5}/(s^2 + bs + c)]\eta^n$ and $\psi_{2n+1}(s) = [(2b)^{0.5}s/(s^2 + bs + c)]\eta^n$, where $\eta = (s^2 - bs + c)/(s^2 + bs + c)$. The time domain counterparts (inverse Laplace transforms) of the functions $\{\psi_n\}$ form a complete orthonormal set $\{\psi'_n\}$ [37]. The complex radian frequency s is related to the vibrational radian frequency ω as $s = j\omega$, where j is the unit imaginary. The two real parameters b and c scale *all* orders of this basis set. They are chosen here to model the resonance frequency and the damping factor of the strongest resonance of polystyrene centered at 3052cm^{-1} .

There are different ways to derive a real function for the expansion of spectral phase from the complex Kautz basis functions. Our preliminary studies have shown the best results by taking the imaginary parts of these complex basis functions. As such, we use the imaginary parts of Kautz functions in the rest of this article.

4.1 1D landscapes

The effect of introducing a polynomial phase of $\varphi^{(n)}(\omega) = \varphi_n(\omega - \omega_0)^n/n!$ and scanning the coefficient φ_n for different values of $2 \leq n \leq 6$ is shown in Fig. 3 (left). In the above equation, ω and ω_0 denote the pump frequency and the pump center frequency, respectively. As the phase order increases, the magnitudes of the slopes and curvatures increase at the origin and decrease at the tails of the curves in Fig. 3 (left). The slight asymmetry of the $n = 2$ case is partially attributed to a small interpolation error in the estimation of the optimal phase. The maximum values of individual polynomial phase terms are $\varphi_{2,\max} = 3 \times 10^3 \text{fs}^2$, $\varphi_{3,\max} = 3.1 \times 10^5 \text{fs}^3$, $\varphi_{4,\max} = 1.9 \times 10^7 \text{fs}^4$, $\varphi_{5,\max} = 4 \times 10^9 \text{fs}^5$, and $\varphi_{6,\max} = 5 \times 10^{11} \text{fs}^6$.

The 1D Kautz landscapes corresponding to the first five orders $0 \leq n \leq 4$ is shown in Fig. 3 (right). Contrary to the case of polynomials, these landscapes feature similar behaviors close to the origin and only start to deviate from each other, where the fitness drops to almost 25% of the maximum fitness. They also feature local optima for larger values of the coefficients

$\varphi_{n,\text{Kautz}}$.

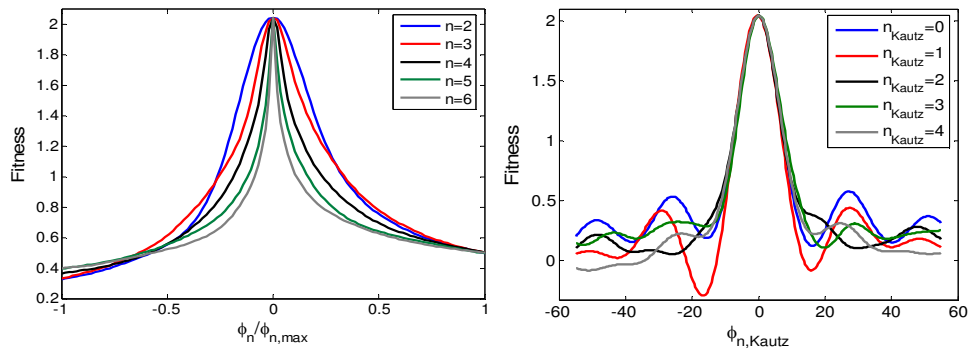


Fig. 3. 1D landscapes around the optimal point with (left) polynomials and (right) Kautz bases.

4.2 2D landscapes

The effect of the simultaneous presence of two polynomial orders in the spectral phase on the landscape is shown in Fig. 4. The two upper rows correspond to phase orders with opposite parities (one even, one odd), and the bottom row corresponds to phase orders with similar parities (both even or both odd). As the phase orders increase, the convexity of the contour lines decreases. The patterns associated with similar-parity orders feature a reduced symmetry, compared to quasi-symmetric patterns of opposite-parity orders. These symmetries are very similar to the 2D polynomial landscapes of another nonlinear process using two shaped photons, namely the second harmonic generation [29,38].

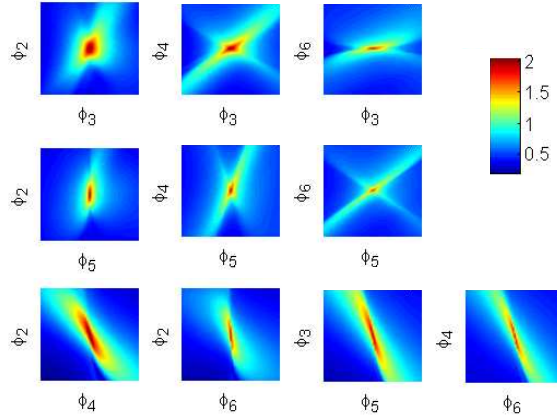


Fig. 4. 2D landscapes around the optimal point with polynomials (top row) even orders of 2,4, and 6 with the third order, (middle) even orders of 2,4, and 6 with the fifth order, and (bottom) orders with similar parities: 2-4, 2-6, 3-5, and 4-6.

The effect of the simultaneous presence of two Kautz functions in the spectral phase on the landscape is shown in Fig. 5. The two upper rows correspond to phase orders with opposite parities, and the bottom row corresponds to phase orders with similar parities. Similar to the case of polynomials shown in Fig. 4, the Kautz landscapes with similar parities have different symmetries and their contours are extended along a line with a negative slope. Similar parities show that two orders with the same sign enhance each other, whereas the same orders with opposite signs partially cancel out each other. Similar to the case of 1D Kautz landscapes, all 2D Kautz landscapes feature a bell-type pattern (red hot spot) at the origin. If the values of the coefficients are limited to this range, the landscapes have more convex contour lines and no local optima, down to smaller values compared to polynomial landscapes.

Note that the considerable overlap of the 1D Kautz landscapes and the overlap of 1D polynomial landscapes at the peaks and also at the tails (Fig. 3) imply reasonably comparable ranges of different phase orders. As such, the elongation of a 2D contour line implies a property of the 2D landscape, and not incomparable ranges of phase terms.

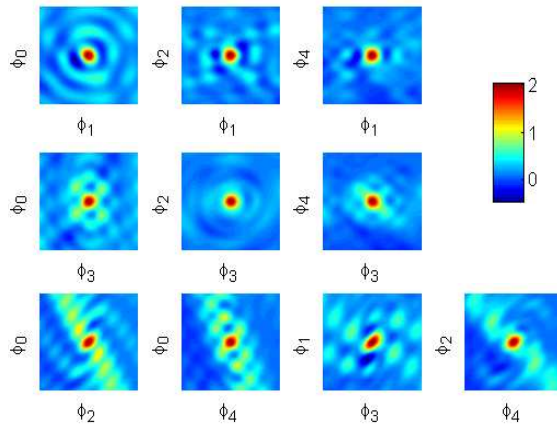


Fig. 5. 2D landscapes around the optimal point with Kautz functions (top row) even orders of 0, 2, and 4 with the first order, (middle) even orders of 0, 2, and 4 with the third order, and (bottom) orders with similar parities: 0-2, 0-4, 1-3, and 2-4.

4.3 3D landscapes

The effect of the simultaneous presence of three orders of Kautz and polynomial functions in the spectral phase (around the optimal phase) on the 3D level sets is shown in Figs. 6(left) and 6(right), respectively. The level sets shown correspond to 56% of the maximum fitness (1.14). Individual level sets associated with polynomials feature more twisted surfaces compared to those of Kautz functions.

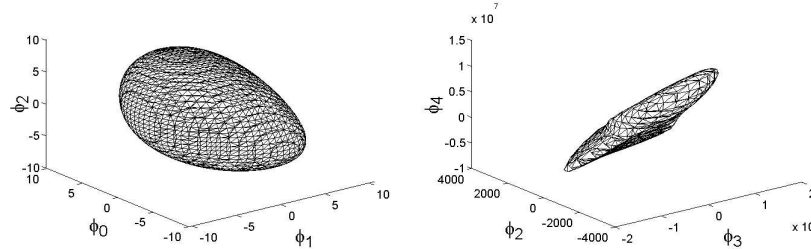


Fig. 6. 3D level sets around the optimal point corresponding to similar fitness values (56% of the maximum fitness) with (left) Kautz and (right) polynomial functions.

4.4 Modified landscapes

We have recently shown that replacing the spectral phase basis of a coherent control experiment with appropriate linear combinations of the basis functions can result in a new landscape with more convex contours, less shear, and even separable phase terms [29,38]. This technique can also be used successfully in the case of a CARS experiment. Figure 7 shows two 2D landscapes (from Fig. 4) and their modified forms, when the third- and the fourth-order polynomials are modified by adding a weighted second-order polynomial to them as $\varphi_{\text{new}}^{(4)}(\omega) = \varphi^{(4)}(\omega) + [-0.91\omega_{\text{FWHM}}^2] \varphi^{(2)}(\omega)$ and $\varphi_{\text{new}}^{(3)}(\omega) = \varphi^{(3)}(\omega) + [0.17\omega_{\text{FWHM}}] \varphi^{(2)}(\omega)$, with $\varphi^{(n)}(\omega)$ defined as in Section 4.1 and ω_{FWHM} denoting the spectrum bandwidth.

Starting from one of such modified contour lines in the vicinity of the maximum point, one can find the projections of the maximum point along each phase coordinate independently. It reduces the required number of measurements for finding the optimal phase in the vicinity of the optimal point from N^2 to $2N$ measurements for a given N points/coordinate resolution.

In each case, the weight factor used in the modified polynomial (-0.91 or 0.17) can be considered as the tangent of the angle between the orientations of the original and modified contour lines. However, note that this transform is a shear and not a rotation of contour lines. This is why the apparent ellipticity of the contour lines has changed. The reader is referred to [29] for a detailed discussion of this topic.

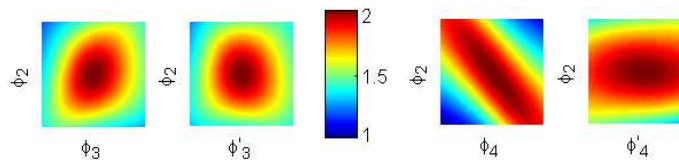


Fig. 7. Modified 2D landscapes obtained by adding a scaled second order polynomial to (left) the third order and (right) the fourth order polynomials.

5. Solution landscapes around the zero point

In this Section, we investigate the landscapes with polynomials and Kautz bases around zero phase, in which case, the pump phase is exactly the phase generated by these basis functions.

5.1 1D landscapes

The 1D landscapes around zero for both polynomial and Kautz basis sets are shown in Fig. 8. Three salient features of these curves, to be contrasted with those of Fig. 3, are anti-symmetry, decreased peak fitness, and non-monotonic variation of the peak fitness as a function of the phase order.

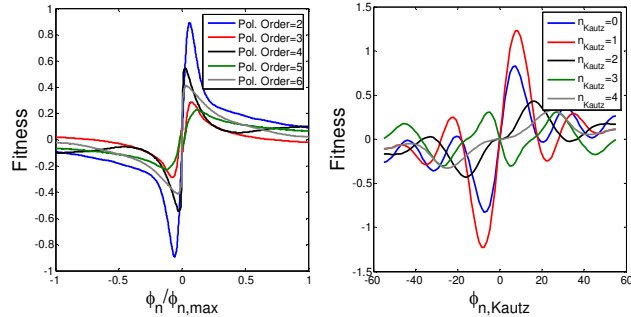


Fig. 8. 1D landscape around the zero phase with (left) polynomials and (right) Kautz bases.

5.2 2D landscapes

The 2D polynomial landscapes around zero are shown in Fig. 9. As in the case of 1D landscapes, two salient differences between these 2D patterns and their counterparts around the optimal phase, shown in Fig. 4, are the change of (quasi) point symmetry to anti-symmetry and also a decreased maximum fitness. However, in the sense of reduced convexity by increased order and also the symmetry differences between similar-parity and opposite-parity phase terms, the patterns of Fig. 9 resemble those in Fig. 4.

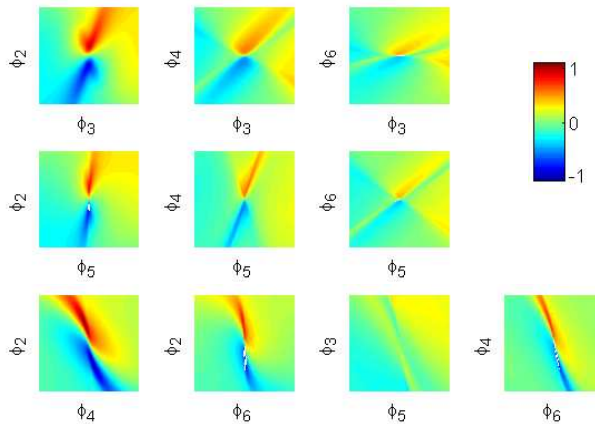


Fig. 9. 2D landscape around the zero phase with polynomials

The 2D landscapes with Kautz functions around the zero phase, shown in Fig. 10, can be compared and contrasted with their counterparts around the optimal phase, similar to the case of polynomials (Fig. 4 vs. Figure 9). The peak fitness of similar-parity landscapes occurs for the second/fourth orders ($n = 1,3$) and not the first two, contrary to polynomial landscapes.

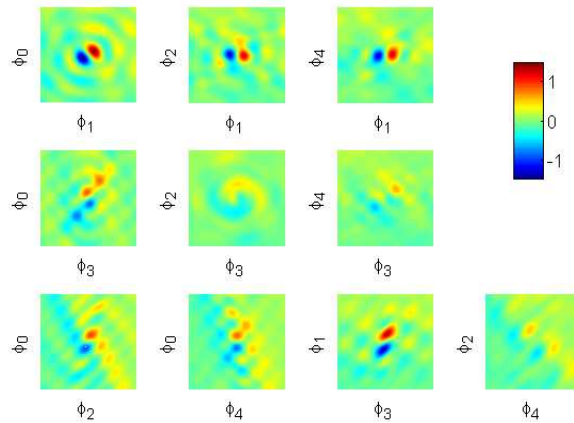


Fig. 10. 2D landscape around the zero phase with Kautz functions

5.3 3D landscapes

The effect of the simultaneous presence of three orders of Kautz and polynomial functions in the spectral phase (around zero) on the 3D level sets is shown in Figs. 11(left) and 11(right), respectively. The level sets shown correspond to 56% of the local maximum fitness in each case (0.85 and 0.61 for Kautz and polynomial functions, respectively). Again, individual level sets associated with polynomials feature more twisted surfaces compared to those of Kautz functions. The 3D level sets around zero achieve maximum fitness values (1.52 for Kautz and 1.07 for polynomial functions) greater than what is achievable in 1D and 2D landscapes, but smaller than that of the optimal point (by 26% in the best case). Kautz

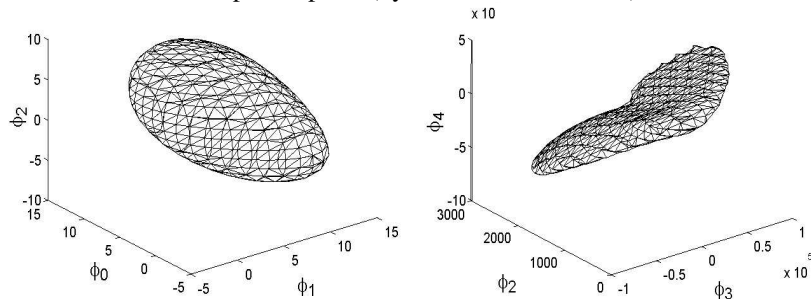


Fig. 11. 3D level sets around the zero point corresponding to comparable fitness values (56% of the local maximum fitness in each case) with (left) Kautz and (right) polynomial functions.

6. Discussion

We have shown the features of different landscapes and compared/contrasted them in previous sections. In this Section, we focus our discussion on the significance and applications of these results.

6.1. Optimization in the lab and efficient use of numerical results

Open-loop scans of Section 5 show that using a few orders of a basis function to achieve the highest fitness is not possible. This observation explains the reduced maximum fitness achieved in closed-loop optimization with a few orders of both polynomial and Kautz functions. As in simulations of Section 3, a successful experimental optimization seems to require a direct parameterization, rather than using a few orders of a basis set. However, such an optimization can be considerably slow because of the relatively high number of optimization parameters, a property referred to as the curse of dimensionality [39]. An

optimal phase profile, such as the one shown in Fig. 2, is obtained within a few minutes by simulation. However, experiment time is limited not by the computational load, rather by the settling time of a phase mask (hundreds of milliseconds) and the large number of laser shots needed to average out noise. It increases the optimization time in the lab by about two orders of magnitude, compared to the time needed to simulate the same optimization. In addition to limiting the number of experiments, each experiment will be more vulnerable to sample degradation, aggregation, and laser drifts and instabilities. Furthermore, such an experiment will be inefficient in the sense of not using the *a-priori* information about optimal phase profile, already obtained by simulation.

An alternative and efficient solution is to use the approach of Section 4; i.e., to use the numerically-obtained optimal phase profile. The numerically-optimal phase may be somehow different from the experimentally-optimal phase, because of the existence of noise, different shaping coordinates, numerical errors, small misalignments, small uncompensated background phase, small instability of the laser source, different level or profile of the non-resonant $\chi^{(3)}$ compared to that used in simulations, existence of impurities, aggregation, and similar factors. In the light of the results of Section 4, using appropriate basis sets such as Kautz functions can overcome this problem by modeling the optimal phase just with a few orders. Furthermore, the orthogonality of basis functions can result in more robustness to noise in adaptive experiments, including adaptive laser pulse shaping [38].

6.2. Chemically-selective measurements

An important practical application of optimized shaped CARS measurements is to employ *characteristic* phase profiles to obtain high-energy background-suppressed resonant signals from specific samples, while suppressing the resonant signals from other samples; i.e., a pattern recognition problem. For simplicity, we restrict ourselves to the case of only two samples, namely polystyrene and PMMA, and only one characteristic phase profile. Using an approach similar to the one introduced in Section 3, we define $F(\varphi) = \|P_{+\varphi}(\omega)\|^2 - \|P_{-\varphi}(\omega)\|^2$, and consider the fitness function to be $F_{\text{norm}} = (F_{\text{PS}}(\varphi) - F_{\text{PMMA}}(\varphi)) / (|F_{\text{PS}}(\varphi_{\text{PS-mol}})| + |F_{\text{PMMA}}(\varphi_{\text{PMMA-mol}})|)$, where $\varphi_{\text{X-mol}}$ denotes the phase of the molecular response, in each case. Again, the aim of the optimization process is to maximize the fitness function. The term in the denominator is just a normalization constant, and can be replaced by alternative terms by simply scaling the fitness.

The optimal phase $\varphi_{\text{PS-PMMA}}$, obtained using the procedure detailed in Section 3, along with the phase profiles of polystyrene and PMMA molecular responses and also the shifted pump spectrum are shown in Fig. 12 (left). As in Fig. 2, the pump spectrum has been shifted by an amount equal to the Stokes frequency for better understanding of its significance at vibrational frequencies. A similar non-resonant background level as before has been considered for both PMMA and polystyrene. Qualitatively, the optimal phase tends to cancel out the phase of polystyrene, while enhancing the phase of PMMA, as expected.

Different implementations of the same optimization goal result in somehow different “optimal” solutions. In general, if $f(x,y)$ is a monotonically increasing/decreasing function of x/y , using $f(F_{\text{PS}}(\varphi), F_{\text{PMMA}}(\varphi))$ is a reasonable way of quantifying our optimization goal. Consider $f = (F_{\text{PS}}(\varphi) - \mu F_{\text{PMMA}}(\varphi)) / [F_0(1 + \mu)]$, where F_0 is a normalization constant, and μ is a dimensionless parameter. For $\mu = 0$, the optimization merely tries to enhance the polystyrene CARS signal, and for $\mu = \infty$, it merely tries to decrease the PMMA CARS signal. The optimization shown in Fig. 12 (left) with $\mu = 1$ seems to balance these two goals by giving similar weights to both polystyrene signal enhancement and PMMA signal suppression. Other intermediate fitness functions, corresponding to finite positive values of μ , also consider both goals but by considering different significances for them. The effect of changing the parameter μ is shown in Fig. 12 (right). It is seen that the optimization is indeed insensitive to μ for values close to 1, where the difference between PS and PMMA signals is maximized. Comparing the fitness values associated with extreme cases of $\mu = 0$ and $\mu = \infty$ indicates that

this optimization is indeed more about decreasing the PMMA CARS signal, rather than enhancing the polystyrene CARS signal.

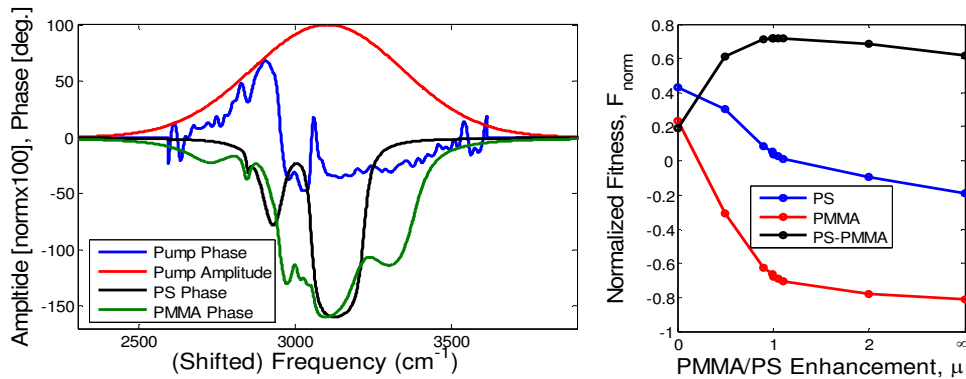


Fig. 12. (Left) Optimal phase profile for enhancing the background-suppressed CARS signal from polystyrene and reducing the corresponding signal from PMMA, and (right) the effect of giving different weights to the CARS energies of PMMA and polystyrene in the definition of the fitness function. The optimized profile shown in black in the left panel corresponds to the case of $\mu = 1$. Solid lines on the right panel are just guides to the eye. The right panel has a linear scale in the interval $[0,2]$.

Characteristic phase profiles can also be used with samples having Raman resonances at vibrational frequencies other than the $\sim 3000\text{cm}^{-1}$ range, such as the fingerprint region. One solution is to use different laser sources with the same CARS scheme. Another solution is to use alternative CARS schemes probing the wavenumbers of interest, with optimized phase profiles. For example, instead of applying a sinusoidal phase and scanning its frequency [9], characteristic phase profiles can be used to excite all Raman lines of a reference sample (and suppress those of other reference samples) to optimize the constructive (destructive) interferences in the time domain. CARS signals from an unknown sample with the so-obtained optimal profiles can potentially determine the type of the sample by fewer measurements and an improved contrast, compared to the approach using a sinusoidal phase.

6.3. Modeling multiple resonances

Analytical techniques and models for system identification have been known for decades in the context of linear system theory and related fields. Fitting experimental data to these models with robustness to numerical and physical noise, especially for higher-order systems, is the subject of an ongoing research, though [40,41]. One of the developments in linear system identification and control is the use of orthogonal rational functions [36]. Here we show that CARS, as a dynamic nonlinear process, can also benefit from such basis sets to model not only a single resonance (Kautz basis), but also multiple Lorentzian Raman resonances by using the orthogonal Takenaka basis set [36]. Note that orthogonality in the context of rational functions is slightly different from that of real functions, as the overlap integral between two functions is performed as a path integral in the complex plane.

The continuous complex frequency variable s , used with Kautz functions, is first mapped via a bilinear transform to another complex frequency variable associated with a discrete system: $z = (1 + sT/2)/(1 - sT/2)$, where T is the grid size of the discrete time series, and s and z are original and modified complex frequencies [36]. Using a temporal sampling of $T = 8.14\text{fs}$, as in our previous simulations, we model not only the dominant Raman peak of polystyrene at 3052cm^{-1} , but also the second Raman peak at 2906cm^{-1} with an amplitude equal to 37% of the main peak. The bilinear transform maps the complex conjugate pairs associated with these two peaks to the interior of the unit circle ($|z| < 1$) at $z_{1,2} = -0.6531 \pm j0.7553$ and $z_{3,4} = -0.6594 \pm j0.7400$, respectively. We use a modified Takenaka basis for the case of complex conjugate pairs [42], and consider equal weights for ψ_{z_i} and $\psi_{z_i^*}$, the basis functions

associated with any complex conjugate pair of poles $\{z_i, z_i^*\}$. By further assuming a similar weight for both complex conjugate pairs $z_{1,2}$ and $z_{3,4}$, we express the spectral phase as $\varphi = \eta \cdot \text{Im}\{\psi_1 + \psi_2 + \psi_3 + \psi_4\}$, where η is a real weight factor, and $\text{Im}\{\}$ denotes the imaginary part of a complex number.

By choosing $\eta = -0.06325$, a high fitness equal to 90% of the maximum fitness is obtained. This is considerably higher than the maximum fitness obtained by polynomials or Kautz functions with one (Fig. 8) or even more (Figs. 9-11) degrees of freedom. A detailed description of the CARS landscapes modeled by this basis and the associated numerical and sampling considerations are beyond the scope of this article, and will be addressed separately.

6.4. Comparison of different bases

The 2D landscapes around the optimal phase corresponding to rational functions (Fig. 5) have the advantage of featuring convex and connected contours down to relatively small values of fitness (27% of the maximum fitness for the first two Kautz orders) in the vicinity of the optimal phase. These contours span similar ranges along each coordinate by choosing the same range for different dimensionless weights of Kautz orders.

The 2D landscapes associated with (lower order) polynomials (Fig. 4) do not feature local minima down to even smaller values of fitness. However, the contours show considerable deviation from a convex pattern (contrast Figs. 5 and 4). As the polynomial orders increase, both similar-parity and opposite-parity 2D landscapes show modulated fitness surfaces close to the maximum point. The depth of modulation increases with polynomial orders. For the φ_3 - φ_5 landscape, the first local maxima occur at 93% of the maximum fitness. These issues associated with polynomial landscapes can be partially resolved by using linear combinations of basis functions [29], as shown in Fig. 7. Also, the 3D level sets associated with polynomial landscapes feature more distortions compared to those associated with rational Kautz functions.

Similar superiority of rational functions to polynomials in modeling phase (aside from local optima) is observed for shaping around the zero phase. Rational functions feature more convex contour lines and higher fitness values compared to polynomials (74% and $\geq 90\%$ of the maximum fitness for Kautz and Takenaka, as opposed to 53% of the maximum fitness for polynomials).

7. Conclusions

In conclusion, we have explicitly addressed the fundamental question behind shaped CARS optimizations, namely the shape and the topology of the solution space contours. We use an evolutionary algorithm to traverse the solution space and find optimal spectral profiles. We then use different basis sets to explore the 1D, 2D, and 3D landscapes around the optimal points and also around zero. The shapes, symmetries, and topologies of the contour lines are discussed in the 1D, 2D, and 3D cases. We demonstrate and highlight the significance of using modified basis functions and alternative orthogonal basis sets to achieve more convex, connected, shear-free contour lines with separable phase terms, and high fitness values with a few (or even a single) basis functions.

Acknowledgements

We thank Dr. Thomas Bäck, Mr. Lars Willmes, Dr. Riccardo Fanciulli, Dr. Janne Savolainen, and Mr. Daan P. Sprünken for their earlier helps with the implementation and interpretation of the algorithm. This research has been supported by the Stichting voor Fundamenteel Onderzoek der Materie (FOM, grant number 03TF78-3), which is supported financially by *Nederlandse Organisatie voor Wetenschappelijk Onderzoek* (NWO).